

Direct Tests of Black Hole Accretion Rate Prescriptions: I. Bondi Accretion at Different Scales

JAMES AGOSTINO,¹ MING-YI LIN,¹ NATASHA JONES,¹ ANNE M. MEDLING,¹
LORETO BARCOS-MUÑOZ,^{2,3} DANIEL ANGLÉS-ALCÁZAR,⁴ CLAUDIO RICCI,^{5,6} GEORGE C. PRIVON,^{7,8,9}
VIVIAN U,^{10,11} PAUL TORREY,^{12,13,14} PHILIP F. HOPKINS,¹⁵ AND CLAIRE MAX¹⁶

¹*Ritter Astrophysical Research Center and Department of Physics & Astronomy, University of Toledo, Toledo, OH 43606, USA*

²*National Radio Astronomy Observatory, 520 Edgemont Road, Charlottesville, VA, 22903, USA*

³*Department of Astronomy, University of Virginia, 530 McCormick Road, Charlottesville, VA, 22903, USA*

⁴*Department of Physics, University of Connecticut, 196 Auditorium Road, U-3046, Storrs, CT 06269, USA*

⁵*Instituto de Estudios Astrofísicos, Facultad de Ingeniería y Ciencias, Universidad Diego Portales, Avenida Ejercito Libertador 441, Santiago, Chile*

⁶*Kavli Institute for Astronomy and Astrophysics, Peking University, Beijing 100871, China*

⁷*National Radio Astronomy Observatory, 520 Edgemont Road, Charlottesville, VA 22903*

⁸*Department of Astronomy, University of Florida, P.O. Box 112055, Gainesville, FL 32611, USA*

⁹*Department of Astronomy, University of Virginia, 530 McCormick Road, Charlottesville, VA 22904, USA*

¹⁰*4129 Frederick Reines Hall, Department of Physics and Astronomy, University of California, Irvine, CA 92697, USA*

¹¹*IPAC, California Institute of Technology, 1200 East California Boulevard, Pasadena, CA 91125, USA*

¹²*Department of Astronomy, University of Virginia, 530 McCormick Road, Charlottesville, VA 22904*

¹³*Virginia Institute for Theoretical Astronomy, University of Virginia, Charlottesville, VA 22904, USA*

¹⁴*The NSF-Simons AI Institute for Cosmic Origins, USA*

¹⁵*TAPIR, Mailcode 350-17, California Institute of Technology, Pasadena, CA 91125, USA*

¹⁶PLACEHOLDER

ABSTRACT

We present spatially resolved parsec-scale measurements of nuclear conditions (gas density and kinetic temperature) relevant for black hole accretion rate predictions in the Seyfert 2 galaxy, NGC 1068. We inject these parameters into the prescription for a Bondi-like accretion model, then compare the resulting accretion rate prediction to the empirical accretion rate derived from hard X-ray observations. Cosmological simulations have spatial resolution ranging between, from ~ 10 pc to on order kpc, and so for reasonable comparison we test these accretion rate predictions in pixel-sized radial steps out to 500 pc. Compared to warm H₂ gas, CO gas is the dominant mass carrier close to the SMBH. We find that the Bondi accretion rate (\dot{M}_{Bondi}) of cold molecular gas alone (measured using CO) overestimates the true accretion rate by up to 4 dex in a small aperture ($r \lesssim 6$ pc) around the black hole, but that it performs much better on large ($r \gtrsim 300$ pc) scales. These results are the first in a series of direct tests of accretion rate prescriptions, and they suggest that using a Bondi accretion formalism to model supermassive black hole accretion in Seyfert 2 galaxies may lead to overestimated accretion rates depending on the resolution of the simulation.

1. INTRODUCTION

Supermassive black holes (SMBHs), despite their small gravitational radius of the sphere

of influence ($1\sim 100$ pc), are thought to be a key piece of the connection between pc and kpc scales of galaxy evolution. Observations of galaxies with active galactic nuclei (AGN) have shown both directly and indirectly that AGN can inject energy into their surrounding environments, which can ultimately quench or in some cases trigger star formation (see [Fabian 2012](#) for a review).

Active galactic nuclei do not only interact with the central part of galaxies, they may also significantly impact several global properties of galaxies and their surrounding intergalactic media, allowing us to indirectly infer their influence on those observables. Relationships between black hole mass and global galaxy properties, like the velocity dispersion of stars in the galactic bulge, have been well-calibrated and show tight correlations (see [Kormendy & Ho 2013](#); [McConnell & Ma 2013](#) for reviews). These correlations suggest that AGN radiative feedback, which in part depends on black hole mass, may leave an imprint on bulge stellar velocity dispersion (see [Ferrarese & Merritt 2000](#); [Gebhardt et al. 2000](#) for seminal studies). Star formation in massive halos is suppressed (e.g. in [Behroozi et al. 2013](#); [Torrey et al. 2014](#)), which could be caused by heating of the interstellar medium (ISM) from AGN feedback. In the high energy regime, a discrepancy is found between the observed and expected correlations between X-ray luminosities and temperatures of gas in the intra-cluster medium (called the L_X -T relation, see [Mushotzky 1984](#); [Markevitch 1998](#)). This discrepancy suggests that gas in the intra-cluster medium evolves differently from dark matter; energetics input by host AGN could be a factor as to why.

Indirect cases of the impact of AGN feedback on galaxy formation histories are only made more intriguing by direct evidence of AGN feedback. Since more than 100 years ago ([M87](#); [Curtis 1918](#)) radio jets powered by a central SMBH

have been seen to extend up to ~ 0.9 Mpc outside from their host galaxies (e.g. Centaurus A; [Burns et al. 1983](#)). Outflows driven by these SMBHs have been observed in the process of depleting the ISM at outflow rates of $700 M_\odot \text{ yr}^{-1}$ (e.g. in Mrk 231; [Feruglio et al. 2010](#)). Our pilot galaxy for this study, NGC 1068, has a complex and well studied AGN-driven outflow that also impacts the ISM on sub-kpc scales (e.g. [Wilson & Ulvestad 1983](#); [Müller-Sánchez et al. 2011](#); [García-Burillo et al. 2014](#); [Saito et al. 2022](#); [Hviding et al. 2023](#); [Holden & Tadhunter 2023](#); [Gallimore & Impellizzeri 2023](#); [Mutie et al. 2024](#); [Hagiwara et al. 2024](#)).

The energy output of an AGN is driven by mass accretion onto its accretion disk, fueled by inflows in the nuclei of galaxies. This gas then accelerates to speeds of up to $> 0.1c$ in the accretion disk, and that disk can power radiative outflows. The direct observational feedback can be classified as two mechanisms: radiative (quasar mode) or kinematic (radio mode) ([Fabian 2012](#)). In the quasar mode, occurring when the black hole accretes mass quickly, photons from the accretion disk couple to the ISM, transferring momentum in a powerful jet. In radio mode, accretion onto the disk is slower, and the primary feedback mechanism is in the form of collimated radio jets that typically appear narrower than quasar-mode jets (see [Cielo et al. 2018](#) for a simulated comparison between the feedback of the two modes). Both modes can drive outflows, but the quasar-mode is thought to start the quenching process (the spatial extent of which grows over time) and then the radio-mode maintains that quenched state (see [Fabian 2012](#) and [Morganti 2017](#) for reviews).

As simulations of galaxy evolution have been informed by increasingly detailed observations, theorists have begun to study the physical mechanisms that drive AGN feedback and how that feedback impacts the simulated host galaxies. [Dubois et al. \(2013a\)](#) (see also [Dubois et al.](#)

228 2013b; Taylor & Kobayashi 2015) examined how
 229 AGN jets impact cold gas and transform blue,
 230 disk galaxies into red ellipticals. Building on
 231 these studies, Rosas-Guevara et al. (2015), who
 232 simulated accretion in galaxies of varied halo
 233 mass, find that in galaxies with M_{Halo} above
 234 $10^{11.5} M_{\odot}$, as was observed in Behroozi et al.
 235 (2013), star formation is suppressed by AGN
 236 feedback. Valentini et al. (2020) perform a suite
 237 of cosmological simulations in which they couple
 238 AGN feedback to different phases of the ISM.
 239 They find, in part, that energy output from the
 240 AGN as feedback must couple with both the
 241 cold and hot phases in order to avoid excessive
 242 SMBH growth.

243 As is seen in both observations and simula-
 244 tions, global galaxy properties can be affected
 245 by accretion-dependent feedback. Theorists
 246 have attempted to model the physical processes
 247 causing those properties to change. Williamson
 248 et al. (2020) perform radiation hydrodynamics
 249 modeling of the 1-100 pc scales in a nuclear re-
 250 gion of a simulated AGN host. They demon-
 251 strate that increasingly polar winds are pro-
 252 duced when anisotropic radiation from the AGN
 253 shifts the mass distribution of the outflow orig-
 254 inating from the AGN. Meenakshi et al. (2022)
 255 simulated the direct interaction between AGN
 256 jet-induced outflows on 2 kpc scale and the ISM
 257 and found shocked emission fronts in the ISM
 258 that could be responsible for stunting star for-
 259 mation. On $r < 1$ pc scale, Wada et al. (2023)
 260 were able to induce radiation-driven dusty out-
 261 flows which impact the ISM as they continue on
 262 their outward paths. Tying the small and large
 263 scales together has been an ongoing challenge.

264 Due to computational constraints, large-scale
 265 cosmological simulations that can model hun-
 266 dreds of Mpc^3 at a time are not able to directly
 267 resolve the physical processes that drive gas ac-
 268 cretion at $<<1$ pc scales where accretion takes
 269 place, and so sub-grid prescriptions for black
 270 hole accretion and its subsequent feedback must

271 be adopted.¹ The ‘sub-grid’ is defined as the re-
 272 gion below the gridded resolution of the simu-
 273 lation. Unfortunately, there is no unified model
 274 for these sub-grid physics, and different stud-
 275 ies use different accretion prescriptions. The
 276 most commonly applied prescription is the one
 277 described in (Bondi 1952), often referred to as
 278 Bondi accretion. The equation follows the form:

$$279 \quad \dot{M}_{\text{Bondi}} = \frac{4\pi G^2 M_{\text{BH}}^2 \rho}{(c_s^2 + v_{\text{rel}}^2)^{3/2}} \quad (1)$$

280 where G is the gravitational constant, M_{BH} is
 281 the mass of the black hole, ρ is the gas density,
 282 c_s is the sound speed, and v_{rel}^2 is the relative
 283 velocity of the gas. In the pure Bondi case, the
 284 gas is assumed to be stationary relative to the
 285 galactic potential, so v_{rel}^2 is zero. This model is
 286 theoretically predicated on gas free-falling onto
 287 the SMBH once it reaches the Bondi radius,
 288 $R_{\text{Bondi}} = 2GM_{\text{BH}}/c_s^2$. The Bondi radius is where
 289 the escape velocity of the SMBH (based on its
 290 mass) equals the sound speed of the gas in the
 291 nuclear region. The physical scale of the Bondi
 292 radius is typically on order 0.1-300 pc if we as-
 293 sume c_s of 400 km s^{-1} and SMBH mass range
 294 of $10^6 \sim 10^9 M_{\odot}$. Some large scale cosmo-
 295 logical simulation suites use a pure Bondi pre-
 296 scription to account for SMBH accretion, like
 297 *MassiveBlack-II* (Khandai et al. 2015), *EAGLE*
 298 (Schaye et al. 2015), and *IllustrisTNG* (Wein-
 299 berger et al. 2017; Pillepich et al. 2018a).

300 Physically, the issue with the Bondi accre-
 301 tion formalism is that it ignores both the angu-
 302 lar momentum of the gas and interactions due
 303 to self-gravity between gas particles, which is
 304 only appropriate in the case of hot, virialized
 305 gas (Hobbs et al. 2012). Recent studies have
 306 shown that gas and other accreting material still

¹ Although there is also much variation in AGN feedback prescriptions, this program will focus on discussing the accretion rate prescriptions, on which all feedback depends.

has angular momentum inside what may be the Bondi radius, particularly in gas-rich mergers or galaxies with Seyfert AGN (e.g. in Davies et al. 2004; Hicks et al. 2013; Medling et al. 2014; Lin et al. 2016), and so Bondi accretion timescales may be much shorter than in reality where angular momentum delays accretion.

To account for this problem, some large-scale cosmological simulation suites apply accretion physics by using modified versions of Bondi accretion. The prescription in the *Illustris* (the predecessor to *IllustrisTNG*; Vogelsberger et al. 2013; Genel et al. 2014) and *Magneticum Pathfinder* hydrodynamical simulation suites (Hirschmann et al. 2014; Bocquet et al. 2016; Dolag et al. 2016) modify Bondi by multiplying Equation 1 by a constant (unitless) ‘boost’ factor α (following the prescription of Springel et al. 2005; Di Matteo et al. 2005; Springel & Hernquist 2005). The boost factor is used to account for the volume average of the Bondi-rates for both the cold and hot phases in the simulations and typically has a value = 100. Another large-scale cosmological model, *Horizon-AGN* (Dubois et al. 2016), uses an α similar to *Illustris* and *Magneticum*, but instead of a constant value, their boost factor (following the prescription from Booth & Schaye 2009) depends on density of the gas. Another approach, used by the large-scale *Romulus* suite (Tremmel et al. 2017) is to adjust the Bondi accretion rate depending on the motion of the simulated gas particles. In *Romulus*, if the smallest relative velocity (which they equate to v_{bulk} , the bulk motion of the gas) of the gas particle closest to the SMBH is faster than the rotational velocity of the gas, they replace the relative velocity of the SMBH with v_{bulk} and multiply the Bondi rate by a boost factor dependent on gas density. Bondi or Bondi-like accretion prescriptions are the most commonly used, but theorists have also designed accretion prescriptions with very different underlying physics. One large-scale

simulation ($[100 h^{-1} \text{ Mpc}]^3$ volume) suite that in part uses one of these prescriptions is *SIMBA* (Davé et al. 2019a). In *SIMBA*, pure Bondi accretion is still applied for hot gas accretion where, as we mentioned, it is most appropriate. But, they then apply a torque-limited accretion formalism for the cold gas where instabilities in the disk drive mass inflow (Hopkins & Quataert 2011; Anglés-Alcázar et al. 2017). Understanding if and in which cases different sub-grid prescriptions are accurately estimating accretion rates onto the black holes of galaxies is critically important to cosmological simulations. *Without an accurate prescription for accretion over time, simulations cannot accurately implement the impact of AGN feedback, and as such may have incorrect outcomes with regards to galaxy formation and evolution.*

Observationally testing how black hole accretion rate prescriptions perform has only become possible in recent times. In this study, we directly measure the parameters that go into Bondi accretion, ρ_{gas} and c_s , on physical scales ranging from 2-170 pc. We then plug these measured parameters into the pure Bondi accretion prescription as a function of radius to mimic what a simulation at that resolution would estimate for the black hole accretion rate. Finally we test these predicted Bondi accretion rates against empirically derived accretion rates using hard (14-195 keV) X-ray data from the The Burst Alert Telescope (BAT) AGN Spectroscopic Survey (BASS) survey (Ricci et al. 2017). The BAT instrument (Barthelmy et al. 2005; Krimm et al. 2013) on *Swift* (Gehrels et al. 2004) is a hard X-ray detector that surveys the entire sky, reporting X-ray sources to within 1-4 arcmin accuracy.

In this work, we use cosmological parameters of $H_0 = 70 \text{ km s}^{-1} \text{ Mpc}^{-1}$, $\Omega_m = 0.28$, and $\Omega_\Lambda = 0.72$ (Hinshaw et al. 2009). To calculate spatial scales and luminosity distance to NGC

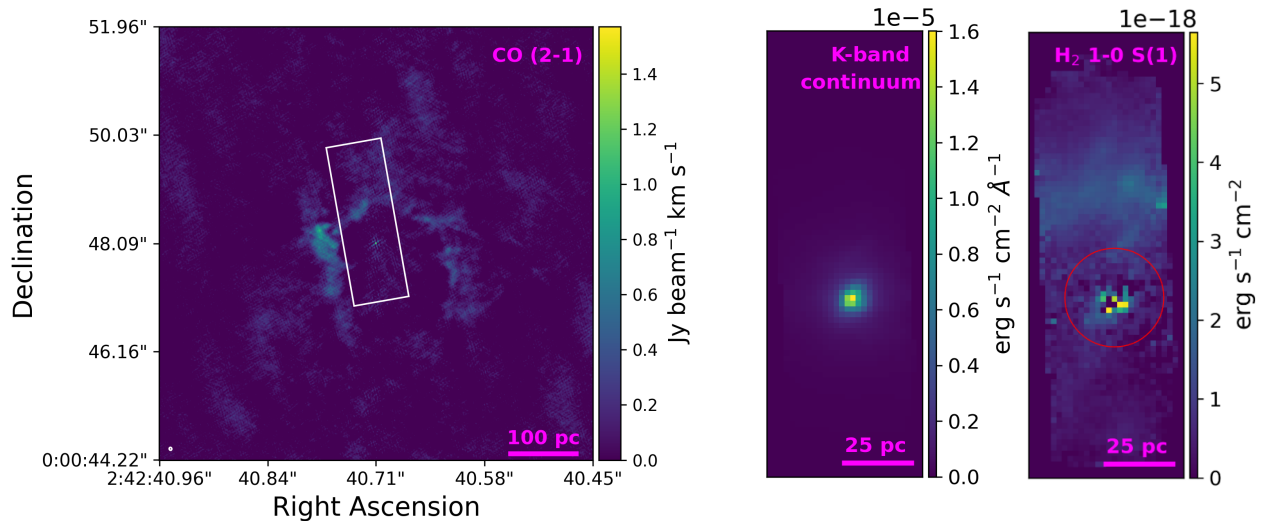


Figure 1. Nuclear region of NGC 1068 in the CO(2-1) flux (left, from ALMA), $2.2\mu\text{m}$ continuum (middle), and the continuum subtracted rovibrational H_2 1-0 S(1) transition (right), described in Section 2. The CO(2-1) moment 0 map is masked below $3\times\text{rms}$ and the white box in the CO(2-1) moment map represents the field of view of the NIR data. The very small, white ellipse in the bottom left represents the beam size of the ALMA data (41×30 mas). All three images show flux peaks at the AGN’s location and both the CO and H_2 maps have enhanced emission in the CND ring. The red circle in the H_2 1-0 S(1) moment map represents the aperture in which T_{Kin} is calculated in Figure 3.

1068 we use Ned Wright’s Cosmology Calculator (Wright 2006).

2. NGC 1068 OBSERVATIONS

For NGC 1068, we made use of <3 pc scale resolution both in the near infrared (NIR) with Keck/OSIRIS+AO (adaptive optics; PI Medling), and in the sub-mm with ALMA archival data (PI García-Burillo).

2.1. Keck/OSIRIS K-band Integral Field Spectroscopy

The first of two sets of data we are using in this project is a set of high resolution integral field unit (IFU) Keck/OSIRIS+AO (OH-Suppressing InfraRed Imaging Spectrograph, Larkin et al. 2006) integrations, for which we mosaic all frames into a single data cube. These observations were taken with the Kbb filter (broad-band K between $1.965 - 2.381\mu\text{m}$) with the 35 mas pixel^{-1} plate scale on 2018 December 28th, 2019 January 22nd, and 2019 October 7th for a total exposure time of 6120 seconds

(51 frames, 120 seconds each). Weather impacted observations on 2019 October 7th, during which the laser guiding system was also not working. We used the galaxy nucleus as the natural guide star in NGS mode, and as the tip/tilt star in LGS mode. AO corrections in those frames without the laser produced larger point spread functions with full-width at half-maximum (FWHM) values between 3 and 5 pixels compared to ~ 2 with the laser on other nights. We reduced the Keck/OSIRIS+AO observations using the OSIRIS Data Reduction Pipeline (OSIRISDRP, Lyke et al. 2017; Lockhart et al. 2019) version 4.2.0, which we use to extract a spectrum for each spatial pixel, assemble the spectra into a cube, and mosaic the 51 total frames together to form the final image, which has a $0.17''$ point spread function (PSF) FWHM. Flux calibration was applied for each night before final mosaicking.

The resulting mosaic reveals a strong K-Band continuum (particularly near the AGN) and

335 H_2 1-0 rovibrational emission ($\text{S}(0)$, $\lambda_{\text{rest}} =$
 336 $2.2235\mu\text{m}$; $\text{S}(1)$, $\lambda_{\text{rest}} = 2.1218\mu\text{m}$; $\text{S}(2)$), $\lambda_{\text{rest}} =$
 337 $2.0338\mu\text{m}$. These continuum and continuum-
 338 subtracted H_2 1-0 $\text{S}(1)$ maps are shown in the
 339 middle and right panels of Figure 1 respec-
 340 tively. The continuum map was made using the
 341 Cube Analysis and Rendering Tool for Astron-
 342 omy (CARTA, Comrie et al. 2021) and the con-
 343 tinuum subtracted H_2 1-0 $\text{S}(1)$ map was made
 344 using QFitsView (Ott 2012). Both images show
 345 peaks of emission on or near the position of the
 346 central engine, and NGC 1068’s circumnuclear
 347 disk (CND) ring can be seen in the H_2 map.

348 2.2. ALMA Band 6 Long-baseline 349 Interferometry

350 We chose the highest resolution CO $J = (2-$
 351 $1)$ (hereafter CO(2-1)) available on the ALMA
 352 archive that shows strong emission (PI García-
 353 Burillo, Project code 2016.1.00232.S; see also
 354 García-Burillo et al. 2019). We retrieved the
 355 CO(2-1) spectral cube product from the ALMA
 356 archive, which has a rms of 0.25 mJy over 20
 357 km s^{-1} , and was imaged using a Briggs (Briggs
 358 1995) robust value of 0, resulting in a beam
 359 size of 41×30 mas. We then used this spec-
 360 tral cube with the image cube analysis tools in
 361 CARTA (Comrie et al. 2021) to create a moment
 362 0 (flux) map of the CO(2-1) emission. Figure 1
 363 (left) shows this CO(2-1) moment 0 map which
 364 is masked below $3 \times \text{rms}$ and is used for our anal-
 365 ysis in Section 3. Like in the warm H_2 observa-
 366 tions, both the AGN and CND ring are bright
 367 sources in CO(2-1).

368 2.3. Nuclear structure of NGC 1068

369 NGC 1068 is one of the most-studied proto-
 370 typical Seyfert galaxies, and as such a wealth of
 371 information has already been published about
 372 its nuclear structure. The studies described here
 373 are not an exhaustive list, but are included to
 374 provide context relevant to our analysis.

375 Under our 2.2 pc resolution, NGC 1068 hosts
 376 a water maser that is thought to originate from

377 the accretion disk on much smaller (<0.1 pc)
 378 scales. Greenhill et al. (1996) observed the
 379 maser with very long baseline interferometry
 380 (VLBI) using both the Very Long Baseline Ar-
 381 ray and Very Large Array to achieve 0.65 pc
 382 resolution. They used the velocity gradient of
 383 the maser emission to infer a rotational velocity
 384 of the gas, and in turn constrain M_{BH} . Kumar
 385 (1999) modeled the 0.65-1.1 pc disk from which
 386 the maser emission is thought to be ejected
 387 from. The clumps in their disk model interact
 388 with each other, leading to eventual accretion
 389 onto the SMBH.

390 On slightly larger scales with near and mid
 391 infrared interferometry, multiple authors were
 392 able to resolve a two-component dusty torus
 393 (Jaffe et al. 2004; Raban et al. 2009). One
 394 component is smaller and more elongated (1.35
 395 $\times 0.45$ pc) in size than the other (3×4 pc).
 396 In the nucleus of Circinus, another Seyfert 2
 397 AGN, Tristram et al. (2014) also found a two-
 398 component dusty torus. Images like these that
 399 showed structure inconsistent with the prior,
 400 observationally-defined, Type 2 classification of
 401 these galaxies (unless foreground extinction was
 402 applied) fundamentally challenged the AGN
 403 unification model (Antonucci 1993).

404 Gámez Rosas et al. (2022) used sub-pc resolu-
 405 tion observations of NGC 1068 taken with the
 406 MATISSE/ESO/VLTI interferometer between
 407 3 and 13 μm to map the dust temperature dis-
 408 tribution of the dust observed in the previously
 409 mentioned studies. They confirm an optically
 410 thick pc scale dusty structure and a second, less
 411 optically thick disk that extends to at least 10
 412 pc. García-Burillo et al. (2019) (who in part
 413 use the same ALMA data as we describe in Sec-
 414 tion 2.2) find a 14 pc CO(2-1) nuclear disk with
 415 a PA (~ 110 -140 deg) aligned with the water
 416 maser disk PA (140 deg). Also in García-Burillo
 417 et al. (2019), they observe the CND, which as
 418 can be seen in Figure 1, has a gas deficit inside
 419 the outer ring in its central ~ 130 pc region.

To resolve the kinematics of the 10 pc inner disk (often referred to as the torus) and outer ring, Imanishi et al. (2020) observe both of these scales using the bright (relative to CO(2-1)) HCN J=(3-2) and HCO+ J = (3-2) transitions with ALMA at 1.4 pc resolution. They find that the torus as observed with these dense gas tracers rotates in the opposite direction with respect to the outer ring. This is particularly surprising because the water maser emission is rotating in the same direction as the outer ring rather than the torus it is physically closer to (see Figure 1 of Imanishi et al. 2020). In the work of García-Burillo et al. (2019), the authors find that a "significant part" of the observed counter-rotation in CO(2-1) can be attributed to a northern AGN-driven wind. To make a more robust determination though, García-Burillo et al. (2019) say that higher resolution data is required so that the outflowing component can be better disentangled from the rotating component.

Outflows originating from the AGN can serve to regulate black hole accretion, and NGC 1068 hosts a complex outflow in the NE direction, perpendicular to the nuclear disk. The largest outflow component is seen as the radio jet (e.g. in Gallimore et al. 1996). Mutie et al. (2024) present higher resolution (~ 4 pc) *e*-MERLIN 5 GHz data along with archival VLA 10 GHz, and VLA 21 GHz images of the jet. These images together show not only the central jet emission, but also detail in the larger scale bow shock, >200 pc from the SMBH in the same NE direction, which exhibits direct evidence of the AGN's impact on the ISM. The impact of the jet on the ISM is studied in part in both Hviding et al. (2023) and Holden & Tadhunter (2023), who both show evidence for gas ionization consistent with shock ionization or radiation-bounded AGN-photoionization along the outflow's path on 160 pc to kpc scale. García-Burillo et al. (2014) show that the CO

kinematics on distances 50 to 400 pc are spatially correlated with the radio jet, evidence that the AGN is influencing even the cold ISM. ALMA CO(6-5) observations from Gallimore et al. (2016) show that this molecular outflow originates within 2 pc from the SMBH, and has velocities relative to systemic of about 400 km s^{-1} . This outflow may have an impact on our measurements of molecular gas mass, but that impact is expected to be small as there is not much CO(2-1) emission between the AGN and CND ring, and the CND ring itself does not appear very disturbed along the path of the outflow.

3. PRESCRIPTION PARAMETERS

In this pilot study, we examine the performance of the most commonly used accretion prescription for black hole growth in NGC 1068. The Bondi accretion formalism with a relative velocity of zero (also known as Bondi-Hoyle, or Bondi-Hoyle-Lyttleton e.g. Hoyle & Lyttleton 1939; Bondi & Hoyle 1944; Bondi 1952) follows the form:

$$\dot{M}_{\text{Bondi}} = 4\pi G^2 M_{\text{BH}}^2 \rho c_s^{-3} \quad (2)$$

where G is the gravitational constant, M_{BH} is the mass of the black hole, ρ is the gas density and c_s is the sound speed.

Bondi accretion is predicated on a spherically symmetric, non-self-gravitating gas distribution in which the gas inside the Bondi radius has no angular momentum. While this kind of environment may not be most appropriate for describing all galaxy nuclei (see Section 5 for additional information), Bondi accretion is a simple analytical prescription that can be applied inside a sphere of any radius, which makes it convenient as a sub-grid prescription.

In this subsection, we outline the methods for measuring each free parameter in the Bondi prescription using the available high resolution data from Section 2.

3.1. Parameter 1: black hole mass

Greenhill et al. (1996) imaged NGC 1068’s water maser emission at a 0.65 pc scale using very long baseline interferometry. From the rotation curve of the water maser emission, they found the enclosed mass within that radius to be $\sim 1 \times 10^7 M_\odot$ (with uncertainty on order unity). Another study by Lodato & Bertin (2003) derive a smaller black hole mass of $\sim 8 \pm 0.3 \times 10^6$ in a self-gravitating accretion disk model that matches the Greenhill et al. (1996) and Greenhill & Gwinn (1997) observations well. The Lodato & Bertin (2003) model corrects for non-Keplerian motion in the velocity profile of the water maser emission, but this could be an over-correction. In fact, other studies have found that the disk rotation may still be dominated by the black hole (Imanishi et al. 2018). Albeit with a worse fit to the velocities from the maser emission, Lodato & Bertin (2003) also fit a Keplerian rotation model, which has a best fit black hole mass of $\sim 1.5 \pm 0.02 \times 10^7 M_\odot$. In the absence of clear evidence in favor of one of the newer modeling schemes, we adopt the Greenhill et al. (1996) value of $M_{\text{BH}} = \sim 1 \times 10^7 M_\odot$ as an intermediate M_{BH} measurement.

3.2. Parameter 2: gas density

3.2.1. Choice of volume element

To measure the gas density, we first must define our volume element. In cosmological simulations, typically, a fixed number gas particles exist inside a spherical region with radius r centered on the location of the SMBH. This volume makes up the black hole kernel, in which the accretion physics are prescribed. Although studies like the ones discussed in Section 2.3 and Vollmer et al. (2022) have shown that ~ 10 pc cold gas distribution is more disk-like, we opt to use a sphere of volume $V = \frac{4}{3}\pi r^3$ centered on the AGN for which we vary the radius with the goal of mimicking the accretion resolution elements found in simulations that use Bondi accretion.

3.2.2. Cold gas mass

To measure the molecular gas (H_2 and He) mass inside the sphere, we use the CO(2-1) data described in Section 2.2. To obtain a molecular gas mass, we utilize the conversion factor α_{CO} . The exact value of α_{CO} depends on several factors including the size scale and environment over which the CO flux is measured. The picture is further complicated by the distinction between $\alpha_{\text{CO}(1-0)}$ and $\alpha_{\text{CO}(2-1)}$, where the difference is dictated by the ratio between the line luminosity of the two rotational transitions: r_{21} ($r_{21} = L'_{\text{CO}(2-1)}/L'_{\text{CO}(1-0)}$), which depends on the temperature of the gas. In this work, we follow the same α_{CO} methodology as in García-Burillo et al. (2019) who use the Milky Way $\alpha_{\text{CO}(1-0)} = 4.3 \pm 1.29 M_\odot (\text{K km s}^{-1} \text{pc}^2)^{-1}$ recommended by Bolatto et al. (2013). We use $\alpha_{\text{CO}(1-0)}$ in conjunction with the averaged line intensity ratios for NGC 1068’s northern and southern CNR regions (because the CNR ring contains the majority of the nuclear gas mass): $r_{21} = 2.2 \pm 0.4$, from Viti et al. (2014) to calculate a final

$$\alpha_{\text{CO}(2-1)} = \frac{\alpha_{\text{CO}(1-0)}}{r_{21}} = \frac{4.3 \pm 1.29}{2.2 \pm 0.4} = 1.95 \pm 0.73 M_\odot (\text{K km s}^{-1} \text{pc}^2)^{-1}. \quad (3)$$

The outflowing components of NGC 1068 may have a lower $\alpha_{\text{CO}(1-0)}$, but we expect the Milky Way value to be closer to the average for the purpose of measuring integrated enclosed masses, especially at larger r . $\alpha_{\text{CO}(2-1)}$ is then multiplied by the sum of the flux density inside a circular aperture of radius r , to match our spherical geometry. The enclosed mass profile is shown alongside a snapshot of the aperture geometry in Figure 2. García-Burillo et al. (2019), who center their $r = 200$ pc aperture measurement on the center of the CNR ring, find a molecular (H_2 + helium) gas mass of $\approx 1.4 \times 10^8 M_\odot$. We measure molecular gas mass within the same aperture (using CARTA to measure flux) and find $1.3 \pm 0.5 \times 10^8 M_\odot$ (1.4

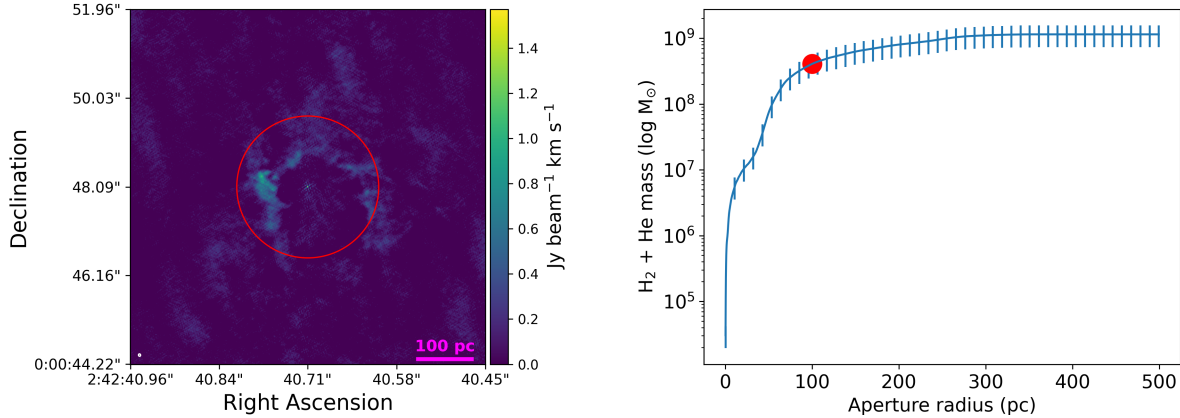


Figure 2. *Left:* Moment 0 map of CO(2-1) in NGC 1068, with flux density values masked below $3 \times \text{rms}$. The red circle indicates the location and size of the 100 pc aperture (centered on the AGN) corresponding to the red dot in the right panel, which has $M_{\text{enc,H}_2+\text{He}} = 4.09 \pm 1.49 \times 10^8 M_\odot$. The small, white ellipse in the bottom left represents the beam size of the ALMA data (41×30 mas). *Right:* Integrated mass profile inside the radial aperture. Details on the conversion to molecular gas mass can be found in Section 3.2.

$\pm 0.5 \times 10^8 M_\odot$ if centered on the AGN), both of which are consistent with the García-Burillo et al. (2019) measurement. For comparison to another nearby Seyfert 2, in the nuclear region of Circinus, using the warm H_2 gas tracer H_2 1-0 S(1), Müller Sánchez et al. (2006) find the total molecular gas mass to be $1.7 \times 10^7 M_\odot$ within $0.8''$ (52 pc). Integrated inside the same physical distance from the SMBH in NGC 1068, we find a molecular gas mass of $8.8 \pm 3.2 \times 10^7 M_\odot$, higher by almost 1 dex.

To convert enclosed mass to density we divide by the volume element for a sphere (see Section 3.2.1) with r defined by our circular aperture size used for measuring mass. In this sphere with $r = 100$ pc centered on the AGN as shown in Figure 2 (left), we find a molecular gas mass density of $93.3 \pm 71.1 M_\odot \text{pc}^{-3}$.

3.2.3. Warm H_2 gas mass

We also calculate an enclosed mass using the warm H_2 gas measured from the NIR data, following Equation 6 of Storch-Bergmann et al. (2009), which uses the line flux of the H_2 1-0 S(1) rovibrational transition at $\lambda_{\text{rest}} = 2.1218 \mu\text{m}$. In NGC 1068, Martins et al. (2010) used the NASA 3-m Infrared Telescope Facil-

ity (IRTF) and found a nuclear (slit $1'' \times 2''$) extinction $E(\text{B-V})$ of 1.13 (from their Table 4). Assuming the standard extinction law of Cardelli et al. (1989) with $R_v = 3.1$, the extinction A_v ($A_v = R_v \times E(\text{B-V})$) is ~ 3.5 . Based on $A_k \sim A_v/10$ (Howarth 1983), the extinction-corrected H_2 gas mass inside $r < 1.7''$ (111 pc) is $\sim 68 M_\odot$, which is about 1.38 times the observed value. The warm H_2 mass is inconsequential compared to the CO-derived value of $4.08 \pm 1.49 \times 10^8 M_\odot$ in the same region.

One reason that the warm gas measurement in this subsection may be so small is due to the radiative environment in NGC 1068's nucleus. Under local thermal equilibrium (LTE, where the energy distribution can be described by a single number locally) conditions, the H_2 emission can be excited by the equilibrium value for temperatures $T \approx 1000$ K (Davies et al. 2005). To reach such high excitation temperatures in NGC 1068, H_2 emission lines can be excited through several mechanisms, as described below:

(1) *UV fluorescence:* This excitation mechanism dominates in photodissociation regions (PDRs). Far-ultraviolet (FUV, $\lambda > 912 \text{ \AA}$) radiation pumps the molecule into electronically ex-

cited states, leading to subsequent cascades that emit fluorescent emission (Wakelam et al. 2017). This mechanism is dominant in Seyfert 1 galaxies (Davies et al. 2005). Although NGC 1068 is classified as a Seyfert 2 galaxy and is expected to have less FUV radiation, the HST/FOC UV image shows a bright nucleus with polarization (Barnouin et al. 2023) within our OSIRIS field of view (FOV).

(2) *Shocks and outflows*: Veilleux et al. (1997) suggest that shocks associated with nuclear outflows are a likely heating source for H₂ in many Seyfert 2 galaxies. May & Steiner (2017) analyzed VLT/SINFONI and Gemini/NIFS data with a larger FOV covering the entire CNB and proposed that the CNB could be an expanding bubble.

(3) *X-ray heating from the AGN*: X-ray emission can penetrate deeply into regions that are opaque to UV photons and influence H₂ excitation (Matt et al. 1997). All of these mechanisms can contribute to H₂ emission.

We measure the H₂ 1-0 S(1) extinction-corrected intrinsic flux ($F_{\text{intrinsic}} = F_{\text{observed}} \times 10^{(0.4A_K)}$) and directly convert it to the warm H₂ gas mass. Due to the rectangular FOV, only an aperture radius of $<0.3''$ is fully contained within the OSIRIS FOV, suggesting that H₂ emission at radii $>0.3''$ is incomplete.

3.3. Parameter 3: sound speed of the gas

The final parameter required in the Bondi accretion formalism is the sound speed of the gas. The sound speed for an ideal gas is:

$$c_s = \sqrt{\frac{\gamma R T_K}{M}} \quad (4)$$

where γ is the adiabatic index (1, as the gas is assumed to be isothermal in each sub-region), R is the gas constant $8.3144598 \text{ J mol}^{-1} \text{ K}^{-1}$, T_K is the temperature of the gas (K), and M is the molar mass (kg) of the gas, for which we assume solar metallicity. All but the temperature in this case are constants.

For the temperature of the molecular gas, we use two methods: one using CO rotation diagrams (cold gas), and another using an excitation diagram for the molecular H₂ (warm gas) from our Keck/OSIRIS+AO NIR data.

3.3.1. CO-derived c_s

For a temperature from CO transitions we refer to the work of Viti et al. (2014) who infer the temperature of the gas in the CNB of NGC 1068 by using CO rotation diagrams. This method assumes that the gas is in LTE, and that the observations are mostly in the Rayleigh-Jeans regime where the intensity of the radiation is proportional to the temperature. This temperature is also known as the ‘rotational temperature’ and is equal to the kinetic temperature if all CO levels are thermalized (Goldsmith & Langer 1999). Because of these assumptions, this temperature should be considered a lower limit, which translates to an upper limit on our final accretion rate because $\dot{M}_{\text{Bondi}} \propto c_s^{-3}$. For the central region of NGC 1068, Viti et al. (2014) find a temperature of $50 \pm 5\text{--}7 \text{ K}$ via the CO rotation diagram method (see Section 3.1.1. of their work for more details). Plugging that and the other constants into Equation 4, we find that the speed of sound in the cold molecular gas phase is $409.2 \pm 141.7 \text{ km s}^{-1}$.

3.3.2. H₂-derived c_s

As shown in Section 3.2.3, warm H₂ is also present in NGC 1068’s nuclear regions, so we also consider the sound speed for this component of the ISM. To measure the temperature which we then use in the c_s calculation, we use the H₂ 1-0 S(0), S(1), and S(2) rovibrational line fluxes in the Keck/OSIRIS NIR data described in Section 2.1. Assuming the H₂ gas is in LTE, the H₂ excitation temperature is equal to the kinetic temperature. Figure 3(a) shows the H₂ excitation diagram, which is the column density in the upper level of each transition normalized by its statistical weight (N_u/g_u) as a function of

energy of the level as a temperature (E_u). The best-fit slope of this relationship is related to T_K as $\frac{N_u}{g_u} \propto e^{(-\frac{h\nu}{kT_K})}$ in the LTE description of energy level populations (see pages 322, 327 of Wilson et al. 2013). Solving for T_K then yields $-\frac{1}{T_K} \propto \frac{\ln \frac{N_u}{g_u}}{\frac{E_u}{k}}$.

Because we have spatially resolved data for these H₂ lines, we can derive kinetic temperatures from 12-111 pc and apply them at the matched distances in the accretion rate prediction. While the Keck/OSIRIS+AO data has a higher resolution than 6 pc, the H₂ 1-0 S(1) and S(2) lines are not detected in a $r \leq 6$ pc (0.1") aperture. Fluxes of the lines are measured using the line fitting tool in QFitsView (Ott 2012), which we use to fit the continuum and one Gaussian component to the integrated (within a region circular region with radius r) spectrum. Figure 3(b) shows the range of excitation temperatures as a function of radius. T_K ranges from 678-2261 K, and peaks at $r \leq 85$ pc where $T_K = 2261^{+3683}_{-1631}$ K. High temperatures may be caused by the influence of the PDR (Section 3.2.2 describes observations of this for NGC 1068), which is found to increase the H₂ 1-0 S(1) emission by up to 70% in the some luminous infrared galaxies (Davies et al. 2000; Davies et al. 2003). Using Equation 4 (with a molar mass of H₂) results in H₂ sound speeds between 1013-1850 km s⁻¹, peaking at $r = 85$ pc.

4. RESULTS: \dot{M}_{Bondi} VS. $\dot{M}_{\text{X-RAY}}$

4.1. Calculating \dot{M}_{Bondi}

Now that we have calculated each parameter for the Bondi accretion prescription in Section 3, we are ready to estimate a Bondi accretion rate. Because our parameters are spatially resolved, we calculate accretion rate as a function of simulated resolution:

$$\dot{M}_{\text{Bondi}}(r) = 4\pi G^2 M_{\text{BH}}^2 \rho(\leq r) c_s(\leq r)^{-3}. \quad (5)$$

Figure 4 shows the Bondi accretion rate for the cold derived case as a function of radius, the

means of which range between about 10^2 and $10^{-3} M_{\odot} \text{ yr}^{-1}$. As the enclosed mass found in Section 3.2 for the warm H₂ gas component in $r < 170$ pc is small (68 M_{\odot}), and the temperature gradient is high (678-2261 K, see Section 3.3.2) relative to the values found for the cold CO gas component, the resulting Bondi accretion rates are much smaller (between about 10^{-10} and $10^{-7} M_{\odot} \text{ yr}^{-1}$) for the warm gas. These results suggest that the cold gas is the dominant carrier of mass accretion on $r < 170$ pc scales. Table 1 shows a range of precise values for both the cold and hot Bondi accretion rates.

4.2. Calculating X-ray accretion rates

To understand how well the Bondi accretion formalism compares to the real accretion rate, we compare it to the X-ray derived accretion rate. To calculate an accretion rate from X-ray measurements, we use *Swift*/BAT data from the BAT AGN Spectroscopic Survey (BASS, Ricci et al. 2017). They present intrinsic luminosities in the 14-195 keV band, which we use alongside the bolometric correction, Equation 17 in Gupta et al. (2024):

$$\log(\kappa_{14-195}) = (0.13 \pm 0.04) \times \log(\lambda_{\text{Edd}}) + (1.04 \pm 0.05) \quad (6)$$

to calculate bolometric luminosity. Because Ricci et al. (2017) measure a neutral column density of $\log N_{\text{H}} = 25.0 \text{ cm}^{-2}$ in NGC 1068 and the X-ray continuum might not be well estimated when the emission is dominated by reprocessed radiation in environments like this, we conservatively estimate uncertainty on the input intrinsic 14-195 keV luminosity to be ± 0.4 dex. We then use that bolometric luminosity in the equation from Netzer & Trakhtenbrot (2014), $L_{\text{bol}} = \eta \dot{M} c^2$, solving for \dot{M} η is the unitless mass-to-radiation conversion efficiency that depends on the spin of the black hole. For stationary, retrograde disk, and maximally rotating SMBHs respectively, the values for η are

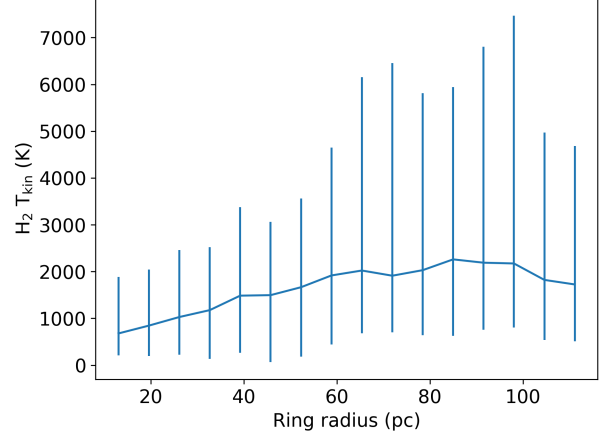
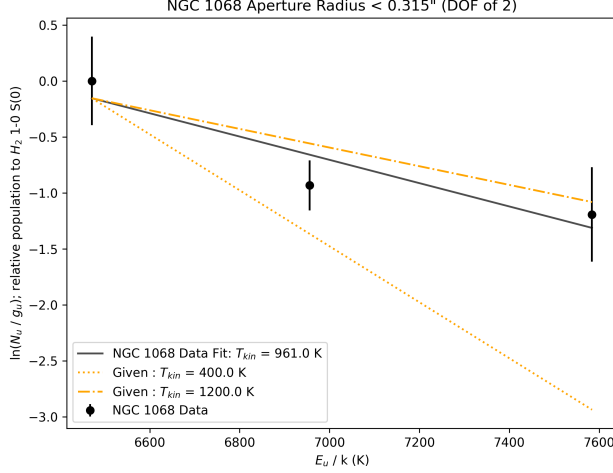


Figure 3. (*Left:*) Column density in the upper level of each H_2 1-0 S(0), S(1), and S(2) transition as a function of energy level of that transition as a temperature (K) inside a $r = 21$ pc circular aperture centered on the AGN as shown in Figure 1. The best fit slope (using linear regression), as described in Section 3.3.2, is the temperature of the gas in that region if we assume LTE. (*Right:*) T_K estimated as in the excitation diagram on the left but instead inside circular apertures matching the methods of Section 3.2 from $0.2''$ to $1.7''$ in steps of $0.1''$. The mean of the derived temperatures is 1612^{+2840}_{-1216} K.

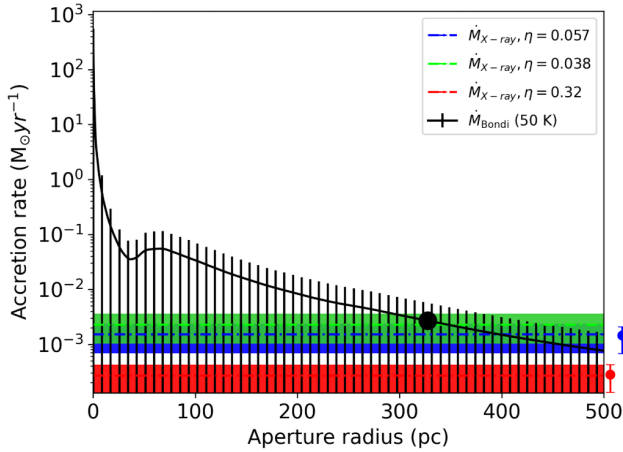


Figure 4. X-ray and (Cold-derived) Bondi accretion rates as a function of radius over which nuclear parameters are measured. Color bars and ranges displayed to the right denote uncertainties on each X-ray measurement. The Bondi prescription overestimates \dot{M}_{BH} by orders of magnitude for low aperture radii, but, above 327 pc (the black circle), the mean Bondi prescription value begins to agree and even dip below the mean minimum prediction from the X-ray by aperture size $r = 398$ pc.

0.057, 0.038, and 0.32 (Netzer & Trakhtenbrot 2014). For NGC 1068, we find $\dot{M}_{\text{X-ray}}$ values

equal to $1.51 \pm 0.81 \times 10^{-3} \text{ M}_{\odot} \text{ yr}^{-1}$ (stationary SMBH), $2.26 \pm 1.21 \times 10^{-3} \text{ M}_{\odot} \text{ yr}^{-1}$ (retrograde accretion disk), and $2.69 \pm 1.43 \times 10^{-3} \text{ M}_{\odot} \text{ yr}^{-1}$ (maximally spinning SMBH). Figure 4 and shown in Table 1. \dot{M}_{Bondi} overestimates the accretion rate by several orders of magnitude at small distances from the SMBH where the gas density is high, but dips below the X-ray accretion rates at large distances, where density is low.

Vollmer et al. (2022) used the IR-derived bolometric luminosity for the AGN in NGC 1068 from Vollmer et al. (2018) to calculate $\dot{M}_{\text{BH}} \sim L_{\text{bol}} / (0.1 c^2) \sim 0.05 \text{ M}_{\odot} \text{ yr}^{-1}$. They calculate a mass accretion rate onto their modeled accretion disk for NGC 1068 to be $2 \times 10^{-3} \text{ M}_{\odot} \text{ yr}^{-1}$ ($\eta = 0.1$), which is in agreement with our $\dot{M}_{\text{X-ray}}$ values and the cold gas derived \dot{M}_{Bondi} in aperture sizes of $r \geq 363$ pc.

5. DISCUSSION: RESULTS IN CONTEXT OF SIMULATIONS

To inform theorists on which accretion prescriptions in their simulations are best to use

Method	Accretion rate ($M_{\odot} \text{ yr}^{-1}$)						
X-rays ($\epsilon = 0.57$)	$1.51 \pm 0.81 \times 10^{-3}$						
X-rays ($\epsilon = 0.38$)	$2.26 \pm 1.21 \times 10^{-3}$						
X-rays ($\epsilon = 0.32$)	$2.69 \pm 1.43 \times 10^{-3}$						
Bondi ($< r$)	5 pc	10 pc	25 pc	50 pc	100 pc	200 pc	500 pc
($T_{\text{Kin}} = 50 \text{ K}$)	1.62 ± 1.79	0.43 ± 0.47	0.06 ± 0.07	0.05 ± 0.05	0.03 ± 0.04	$8.32 \pm 9.16 \times 10^{-4}$	$7.63 \pm 8.41 \times 10^{-4}$
($T_{\text{Kin}} = 678\text{-}2261 \text{ K}$)	*	*	$8.16^{+28.89}_{-21.6} \times 10^{-9}$	$4.95^{+15.87}_{-14.03} \times 10^{-10}$	$5.04^{+23.61}_{-11.20} \times 10^{-11}$	*	*

Table 1. Accretion rate measurements and estimates for rates derived from X-ray luminosities and the pure Bondi accretion prescription inside various radii. In NGC 1068, where the cold gas phase makes up the bulk of the gas mass in the nucleus, the cold gas derived Bondi accretion estimate outpaces the X-ray derived accretion rates by between 2 and 4 orders of magnitude. *H₂ 1-0 S(1) and S(2) lines required to calculate temperature for the Bondi calculation are not detected in this aperture.

and when, we have designed our measurements to fit in the practical context of those simulations. Large scale cosmological simulations must use sub-grid physics for accretion because of computing constraints. Some examples of hydrodynamical galaxy evolution simulations that use or have popular options to use a spherically symmetric, Bondi or Bondi-like black hole accretion formalisms are *Illustris*/*IllustrisTNG* (Genel et al. 2014; Vogelsberger et al. 2014; Pillepich et al. 2018b), *Magneticum Pathfinder* (Hirschmann et al. 2014; Bocquet et al. 2016; Dolag et al. 2016), *MassiveBlack-II* (Khandai et al. 2015), *Eagle* (Schaye et al. 2015), *Horizon-AGN* (Dubois et al. 2016), *Romulus* (Tremmel et al. 2017), and *SIMBA* (Davé et al. 2019b, uses Bondi for hot gas only). The resolution of the hydrodynamical gas cells in which these sub-grid physics are calculated ranges from to 10s of pc to more typically kpc. Even in the highest resolution zoom-in simulations, the spherical radius in which particle calculations are made is approximately 10 pc (Wetzel et al. 2023).

Because we have spatially-resolved measurements, we are able to examine the performance of Bondi accretion at a range of spatial scales. For the Bondi accretion rate derived from warm gas we are limited by the field of view of OSIRIS

($0.56 \times 2.24''$ with our observational setup), but the ALMA data extends to over 500 pc away from the SMBH.

Table 1 shows the Bondi accretion rates at radii between 5-500 pc as calculated in Section 4, and the X-ray accretion rates as calculated in Section 4.2, which are all plotted together in Figure 4. At aperture radii $r \leq 327$ pc, the parameterized Bondi accretion rate exceeds the X-ray derived accretion rate (by 2 or more dex in aperture sizes of $r \lesssim 15$ pc and by 1 or more dex when $r \lesssim 125$ pc).

This is, perhaps, not a surprising result. Past studies have hinted towards Bondi accretion overestimating the real accretion rate. Di Matteo et al. (2000) found that luminosities calculated using estimated Bondi accretion rates for six black holes with masses of $0.22\text{-}5.2 \times 10^9 M_{\odot}$ determined in Magorrian et al. (1998) were 4-6 orders of magnitude higher than the real luminosities of the galaxy nuclei. Hopkins et al. (2016) model SMBH accretion in a gas-rich nuclear disk in a massive simulated galaxy with 0.1 pc resolution. In their study, applying a pure Bondi accretion formalism resulted in an accretion rate $\sim 10^8$ times higher than the luminosity-derived accretion rate native to their simulation. Near the SMBH, pure Bondi accretion ignores

the possibility that gas particles may have angular momentum. The gas in the simulation used in Hopkins et al. (2016) is primarily cold and is supported by angular momentum rather than radiation pressure. Observations show that especially in gas-rich galaxies that naturally host molecular torii, the $r < 100$ pc cold gas reservoir is large, has significant angular momentum, and is the primary candidate for black hole accretion fueling (Davies et al. 2004; Hicks et al. 2013; Medling et al. 2014; Lin et al. 2016; Gaspari et al. 2015). Ignoring the angular momentum of the cold gas is likely the primary cause of the overestimate that Bondi accretion makes both in Hopkins et al. (2016) the aperture sizes of $r \lesssim 327$ pc in this work.

The performance of Bondi accretion between 200-500 pc is more realistic, and it even dips below the X-ray derived accretion rates for very large ($r \geq 398$) apertures. This is because, as is apparent in Figure 2, the cold gas has much lower average densities at large distances from the SMBH.

If NGC 1068 is typical, these results suggest that the usage of pure Bondi accretion is likely to struggle to accurately predict black hole accretion rates. From our example, the accuracy of Bondi predictions depends heavily on the size of the black hole kernel used to calculate nuclear conditions, overpredicting in the small radius limit and underpredicting in the large radius limit. Understanding the physical mechanisms that drive accretion on the sub-grid scales in galactic nuclei can inform the future development of accretion prescriptions. The Bondi prescription applies free-fall to particles inside the Bondi radius, but our results suggest that angular momentum plays an important role in some nuclei.

6. CONCLUSIONS AND FUTURE EXPANSION OF THIS PROJECT

In this study we estimate a Bondi accretion rate as a function of radius for NGC 1068 using

two different molecular gas tracers, and compare the result to the direct accretion rate derived from hard X-ray luminosity of the AGN. Compared to warm H_2 gas, CO gas is the dominant mass carrier close to the SMBH. Following this, the cold gas derived Bondi accretion rate estimate outpaces the X-ray derived value by more than 1 order of magnitude at aperture sizes $r \lesssim 125$ pc and up to 4 dex inside the smallest apertures. In the case of warm gas Bondi accretion where the enclosed mass involved in the calculation is negligible, and in the cold gas case in aperture sizes of $r \gtrsim 327$ pc, the Bondi accretion rate is instead lower than or equal to the X-ray accretion rates.

This paper is a pilot for a wider study of AGN and accretion prescriptions. Direct probes of sub-grid accretion prescriptions may, as our sample expands, help identify which physical processes dominate accretion on a variety of spatial scales, and in turn provide recommendations for appropriate sub-grid prescriptions to describe them. The results in this work support previous evidence that in high resolution cosmological simulations, applying a Bondi accretion prescription can lead to large overestimates of \dot{M}_{BH} and therefore large overestimates of AGN feedback, which in turn impacts the global galaxy evolutionary track. We note that this is a test for a specific Seyfert 2 AGN. To make more robust recommendations about the application of the Bondi accretion prescription for sub-grid accretion physics we must directly test Bondi on more galaxies.

7. ACKNOWLEDGEMENTS

The authors wish to recognize and acknowledge the very significant cultural role and reverence that the summit of Maunakea has always had within the indigenous Hawaiian community; we are privileged to be guests on your sacred mountain. We wish to pay respect to the Atacameño community of the Chajnantor Plateau, whose traditional home now also in-

cludes the ALMA observatory. This work makes use of the following data from ALMA: project 2016.1.00232.S (PI García-Burillo). ALMA is a partnership of ESO (representing its member states), NSF (USA) and NINS (Japan), together with NRC (Canada) and NSC and ASIAA (Taiwan) and KASI (Republic of Korea), in cooperation with the Republic of Chile. The Joint ALMA Observatory is operated by ESO, AUI/NRAO and NAOJ. The National Radio Astronomy Observatory is a facility of the National Science Foundation operated under cooperative agreement by Associated Universities, Inc. Some of the data presented herein were obtained at the W. M. Keck Observatory, which is operated as a scientific partnership among the California Institute of Technology, the University of California and the

National Aeronautics and Space Administration. The Observatory was made possible by the generous financial support of the W. M. Keck Foundation. The authors also wish to thank the W.M. Keck Observatory staff for their efforts on the OSIRIS+AO instrumentation. JA, AMM, M-YL, and NJ acknowledge support from NSF CAREER grant number 2239807 and Cottrell Scholar Award CS-CSA-2024-092 from the Research Corporation for Science Advancement. PT acknowledges support from NSF-AST 2346977 and the NSF-Simons AI Institute for Cosmic Origins which is supported by the National Science Foundation under Cooperative Agreement 2421782 and the Simons Foundation award MPS-AI-00010515.

Software: Astropy (Astropy Collaboration et al. 2013, 2018, 2022), Matplotlib (Hunter 2007), NumPy (Harris et al. 2020).

REFERENCES

- Anglés-Alcázar, D., Davé, R., Faucher-Giguère, C.-A., Özel, F., & Hopkins, P. F. 2017, *MNRAS*, 464, 2840
- Antonucci, R. 1993, *ARA&A*, 31, 473
- Astropy Collaboration et al. 2013, *A&A*, 558, A33
- . 2018, *AJ*, 156, 123
- . 2022, *ApJ*, 935, 167
- Barnouin, T., Marin, F., Lopez-Rodriguez, E., Huber, L., & Kishimoto, M. 2023, *A&A*, 678, A143
- Barthelmy, S. D., et al. 2005, *SSRv*, 120, 143
- Behroozi, P. S., Wechsler, R. H., & Conroy, C. 2013, *ApJ*, 770, 57
- Bocquet, S., Saro, A., Dolag, K., & Mohr, J. J. 2016, *MNRAS*, 456, 2361
- Bolatto, A. D., Wolfire, M., & Leroy, A. K. 2013, *ARA&A*, 51, 207
- Bondi, H. 1952, *MNRAS*, 112, 195
- Bondi, H., & Hoyle, F. 1944, *MNRAS*, 104, 273
- Booth, C. M., & Schaye, J. 2009, *MNRAS*, 398, 53
- Briggs, D. S. 1995, in *American Astronomical Society Meeting Abstracts*, Vol. 187, American Astronomical Society Meeting Abstracts, 112.02
- Burns, J. O., Feigelson, E. D., & Schreier, E. J. 1983, *ApJ*, 273, 128
- Cardelli, J. A., Clayton, G. C., & Mathis, J. S. 1989, *ApJ*, 345, 245
- Cielo, S., Bieri, R., Volonteri, M., Wagner, A. Y., & Dubois, Y. 2018, *MNRAS*, 477, 1336
- Comrie, A., et al. 2021, *CARTA: The Cube Analysis and Rendering Tool for Astronomy*
- Curtis, H. D. 1918, *Publications of Lick Observatory*, 13, 9
- Davé, R., Anglés-Alcázar, D., Narayanan, D., Li, Q., Rafieferantsoa, M. H., & Appleby, S. 2019a, *MNRAS*, 486, 2827
- . 2019b, *MNRAS*, 486, 2827
- Davies, R., Ward, M., & Sugai, H. 2000, *ApJ*, 535, 735
- Davies, R. I., Sternberg, A., Lehnert, M., & Tacconi-Garman, L. E. 2003, *ApJ*, 597, 907
- Davies, R. I., Sternberg, A., Lehnert, M. D., & Tacconi-Garman, L. E. 2005, *ApJ*, 633, 105
- Davies, R. I., Tacconi, L. J., & Genzel, R. 2004, *ApJ*, 613, 781
- Di Matteo, T., Quataert, E., Allen, S. W., Narayan, R., & Fabian, A. C. 2000, *MNRAS*, 311, 507
- Di Matteo, T., Springel, V., & Hernquist, L. 2005, *Nature*, 433, 604

- 1059 Dolag, K., Komatsu, E., & Sunyaev, R. 2016,
 1060 MNRAS, 463, 1797
 1061 Dubois, Y., Gavazzi, R., Peirani, S., & Silk, J.
 1062 2013a, MNRAS, 433, 3297
 1063 Dubois, Y., Peirani, S., Pichon, C., Devriendt, J.,
 1064 Gavazzi, R., Welker, C., & Volonteri, M. 2016,
 1065 MNRAS, 463, 3948
 1066 Dubois, Y., Pichon, C., Devriendt, J., Silk, J.,
 1067 Haehnelt, M., Kimm, T., & Slyz, A. 2013b,
 1068 MNRAS, 428, 2885
 1069 Fabian, A. C. 2012, ARA&A, 50, 455
 1070 Ferrarese, L., & Merritt, D. 2000, ApJL, 539, L9
 1071 Feruglio, C., Maiolino, R., Piconcelli, E., Menci,
 1072 N., Aussel, H., Lamastra, A., & Fiore, F. 2010,
 1073 A&A, 518, L155
 1074 Gallimore, J. F., Baum, S. A., O’Dea, C. P., &
 1075 Pedlar, A. 1996, ApJ, 458, 136
 1076 Gallimore, J. F., & Impellizzeri, C. M. V. 2023,
 1077 ApJ, 951, 109
 1078 Gallimore, J. F., et al. 2016, ApJL, 829, L7
 1079 Gámez Rosas, V., et al. 2022, Nature, 602, 403
 1080 García-Burillo, S., et al. 2014, A&A, 567, A125
 1081 —. 2019, A&A, 632, A61
 1082 Gaspari, M., Brighenti, F., & Temi, P. 2015,
 1083 A&A, 579, A62
 1084 Gebhardt, K., et al. 2000, ApJL, 539, L13
 1085 Gehrels, N., et al. 2004, ApJ, 611, 1005
 1086 Genel, S., et al. 2014, MNRAS, 445, 175
 1087 Goldsmith, P. F., & Langer, W. D. 1999, ApJ,
 1088 517, 209
 1089 Greenhill, L. J., & Gwinn, C. R. 1997, Ap&SS,
 1090 248, 261
 1091 Greenhill, L. J., Gwinn, C. R., Antonucci, R., &
 1092 Barvainis, R. 1996, ApJL, 472, L21
 1093 Gupta, K. K., et al. 2024, A&A, 691, A203
 1094 Hagiwara, Y., Baan, W. A., Imanishi, M., &
 1095 Diamond, P. 2024, MNRAS, 528, 3668
 1096 Harris, C. R., et al. 2020, Nature, 585, 357
 1097 Hicks, E. K. S., Davies, R. I., Maciejewski, W.,
 1098 Emsellem, E., Malkan, M. A., Dumas, G.,
 1099 Müller-Sánchez, F., & Rivers, A. 2013, ApJ,
 1100 768, 107
 1101 Hinshaw, G., et al. 2009, ApJS, 180, 225
 1102 Hirschmann, M., Dolag, K., Saro, A., Bachmann,
 1103 L., Borgani, S., & Burkert, A. 2014, MNRAS,
 1104 442, 2304
 1105 Hobbs, A., Power, C., Nayakshin, S., & King,
 1106 A. R. 2012, MNRAS, 421, 3443
 1107 Holden, L. R., & Tadhunter, C. N. 2023, MNRAS,
 1108 524, 886
 1109 Hopkins, P. F., & Quataert, E. 2011, MNRAS,
 1110 415, 1027
 1111 Hopkins, P. F., Torrey, P., Faucher-Giguère,
 1112 C.-A., Quataert, E., & Murray, N. 2016,
 1113 MNRAS, 458, 816
 1114 Howarth, I. D. 1983, MNRAS, 203, 301
 1115 Hoyle, F., & Lyttleton, R. A. 1939, Proceedings of
 1116 the Cambridge Philosophical Society, 35, 405
 1117 Hunter, J. D. 2007, Computing in Science &
 1118 Engineering, 9, 90
 1119 Hviding, R. E., Hickox, R. C., Väisänen, P.,
 1120 Ramphul, R., & Hainline, K. N. 2023, AJ, 166,
 1121 111
 1122 Imanishi, M., Nakanishi, K., Izumi, T., & Wada,
 1123 K. 2018, ApJL, 853, L25
 1124 Imanishi, M., et al. 2020, ApJ, 902, 99
 1125 Jaffe, W., et al. 2004, Nature, 429, 47
 1126 Khandai, N., Di Matteo, T., Croft, R., Wilkins,
 1127 S., Feng, Y., Tucker, E., DeGraf, C., & Liu,
 1128 M.-S. 2015, MNRAS, 450, 1349
 1129 Kormendy, J., & Ho, L. C. 2013, ARA&A, 51, 511
 1130 Krimm, H. A., et al. 2013, ApJS, 209, 14
 1131 Kumar, P. 1999, ApJ, 519, 599
 1132 Larkin, J., et al. 2006, in Society of Photo-Optical
 1133 Instrumentation Engineers (SPIE) Conference
 1134 Series, Vol. 6269, Ground-based and Airborne
 1135 Instrumentation for Astronomy, ed. I. S.
 1136 McLean & M. Iye, 62691A
 1137 Lin, M.-Y., et al. 2016, MNRAS, 458, 1375
 1138 Lockhart, K. E., et al. 2019, AJ, 157, 75
 1139 Lodato, G., & Bertin, G. 2003, A&A, 398, 517
 1140 Lyke, J., et al. 2017, OSIRIS Toolbox:
 1141 OH-Suppressing InfraRed Imaging
 1142 Spectrograph pipeline, Astrophysics Source
 1143 Code Library, record ascl:1710.021
 1144 Magorrian, J., et al. 1998, AJ, 115, 2285
 1145 Markevitch, M. 1998, ApJ, 504, 27
 1146 Martins, L. P., Rodríguez-Ardila, A., de Souza,
 1147 R., & Gruenwald, R. 2010, MNRAS, 406, 2168
 1148 Matt, G., et al. 1997, A&A, 325, L13
 1149 May, D., & Steiner, J. E. 2017, MNRAS, 469, 994
 1150 McConnell, N. J., & Ma, C.-P. 2013, ApJ, 764, 184
 1151 Medling, A. M., et al. 2014, ApJ, 784, 70
 1152 Meenakshi, M., et al. 2022, MNRAS, 516, 766
 1153 Morganti, R. 2017, Frontiers in Astronomy and
 1154 Space Sciences, 4, 42
 1155 Müller Sánchez, F., Davies, R. I., Eisenhauer, F.,
 1156 Tacconi, L. J., Genzel, R., & Sternberg, A.
 1157 2006, A&A, 454, 481

- 1158 Müller-Sánchez, F., Prieto, M. A., Hicks, E. K. S.,
 1159 Vives-Arias, H., Davies, R. I., Malkan, M.,
 1160 Tacconi, L. J., & Genzel, R. 2011, *ApJ*, 739, 69
 1161 Mushotzky, R. F. 1984, *Physica Scripta Volume*
 1162 *T*, 7, 157
 1163 Mutie, I. M., et al. 2024, *MNRAS*, 527, 11756
 1164 Netzer, H., & Trakhtenbrot, B. 2014, *MNRAS*,
 1165 438, 672
 1166 Ott, T. 2012, QFitsView: FITS file viewer,
 1167 Astrophysics Source Code Library, record
 1168 ascl:1210.019
 1169 Pillepich, A., et al. 2018a, *MNRAS*, 473, 4077
 1170 —. 2018b, *MNRAS*, 473, 4077
 1171 Raban, D., Jaffe, W., Röttgering, H.,
 1172 Meisenheimer, K., & Tristram, K. R. W. 2009,
 1173 *MNRAS*, 394, 1325
 1174 Ricci, C., et al. 2017, *ApJS*, 233, 17
 1175 Rosas-Guevara, Y. M., et al. 2015, *MNRAS*, 454,
 1176 1038
 1177 Saito, T., et al. 2022, *ApJ*, 935, 155
 1178 Schaye, J., et al. 2015, *MNRAS*, 446, 521
 1179 Springel, V., Di Matteo, T., & Hernquist, L. 2005,
 1180 *MNRAS*, 361, 776
 1181 Springel, V., & Hernquist, L. 2005, *ApJL*, 622, L9
 1182 Storch-Bergmann, T., McGregor, P. J., Riffel,
 1183 R. A., Simões Lopes, R., Beck, T., & Dopita,
 1184 M. 2009, *MNRAS*, 394, 1148
 1185 Taylor, P., & Kobayashi, C. 2015, *MNRAS*, 448,
 1186 1835
 1187 Torrey, P., Vogelsberger, M., Genel, S., Sijacki,
 1188 D., Springel, V., & Hernquist, L. 2014,
 1189 *MNRAS*, 438, 1985
 1190 Tremmel, M., Karcher, M., Governato, F.,
 1191 Volonteri, M., Quinn, T. R., Pontzen, A.,
 1192 Anderson, L., & Bellovary, J. 2017, *MNRAS*,
 1193 470, 1121
 1194 Tristram, K. R. W., Burtscher, L., Jaffe, W.,
 1195 Meisenheimer, K., Hönig, S. F., Kishimoto, M.,
 1196 Schartmann, M., & Weigelt, G. 2014, *A&A*,
 1197 563, A82
 1198 Valentini, M., et al. 2020, *MNRAS*, 491, 2779
 1199 Veilleux, S., Goodrich, R. W., & Hill, G. J. 1997,
 1200 *ApJ*, 477, 631
 1201 Viti, S., et al. 2014, *A&A*, 570, A28
 1202 Vogelsberger, M., Genel, S., Sijacki, D., Torrey,
 1203 P., Springel, V., & Hernquist, L. 2013, *MNRAS*,
 1204 436, 3031
 1205 Vogelsberger, M., et al. 2014, *MNRAS*, 444, 1518
 1206 Vollmer, B., Schartmann, M., Burtscher, L.,
 1207 Marin, F., Hönig, S., Davies, R., & Goosmann,
 1208 R. 2018, *A&A*, 615, A164
 1209 Vollmer, B., et al. 2022, *A&A*, 665, A102
 1210 Wada, K., Kudoh, Y., & Nagao, T. 2023,
 1211 *MNRAS*, 526, 2717
 1212 Wakelam, V., et al. 2017, *Molecular Astrophysics*,
 1213 9, 1
 1214 Weinberger, R., et al. 2017, *MNRAS*, 465, 3291
 1215 Wetzel, A., et al. 2023, *ApJS*, 265, 44
 1216 Williamson, D., Hönig, S., & Venanzi, M. 2020,
 1217 *ApJ*, 897, 26
 1218 Wilson, A. S., & Ulvestad, J. S. 1983, *ApJ*, 275, 8
 1219 Wilson, T. L., Rohlfs, K., & Hüttemeister, S.
 1220 2013, *Tools of Radio Astronomy*
 1221 Wright, E. L. 2006, *PASP*, 118, 1711